Non-null full field X-ray mirror metrology using SCOTS: a reflection deflectometry approach

Peng Su,[1,*] Yuhao Wang, [1] James H. Burge,[1] and Konstantine Kaznatcheev,[2] and Mourad Idir[2,3]

[1]*University of Arizona College of Optical Sciences, 1630 East University Boulevard, Tucson, Arizona 85721, USA*
[2]*Brookhaven National Laboratory, NSLS II 50 Rutherford Dr., Upton, New York 11973-5000, USA*
[3]*midir@bnl.gov*
*psu@email.arizona.edu

Abstract: In a previous paper, the University of Arizona (UA) has developed a measurement technique called: Software Configurable Optical Test System (SCOTS) based on the principle of reflection deflectometry. In this paper, we present results of this very efficient optical metrology method applied to the metrology of X-ray mirrors. We used this technique to measure surface slope errors with precision and accuracy better than 100 nrad (rms) and ~200 nrad (rms), respectively, with a lateral resolution of few mm or less. We present results of the calibration of the metrology systems, discuss their accuracy and address the precision in measuring a spherical mirror.

©2012 Optical Society of America

OCIS codes: (120.3940) Metrology; (340.0340) X-ray optics; (340.7470) X-ray mirrors; (340.6720) Synchrotron radiation.

References and links

1. W. Chao, J. Kim, S. Rekawa, P. Fischer, and E. H. Anderson, "Demonstration of 12 nm resolution Fresnel zone plate lens based soft x-ray microscopy," Opt. Express **17**(20), 17669–17677 (2009).
2. A. Snigirev, V. Kohn, I. Snigireva, A. Souvorov, and B. Lengeler, "Focusing high-energy x rays by compound refractive lenses," Appl. Opt. **37**(4), 653–662 (1998).
3. C. G. Schroer, P. Boye, J. M. Feldkamp, J. Patommel, A. Samberg, A. Schropp, A. Schwab, S. Stephan, G. Falkenberg, G. Wellenreuther, and N. Reimers, "Hard X-ray nanoprobe at beamline P06 at PETRA III," Nucl. Instrum. Methods Phys. Res. A **616**(2-3), 93–97 (2010).
4. S. Matsuyama, T. Wakioka, N. Kidani, T. Kimura, H. Mimura, Y. Sano, Y. Nishino, M. Yabashi, K. Tamasaku, T. Ishikawa, and K. Yamauchi, "One-dimensional Wolter optics with a sub-50 nm spatial resolution," Opt. Lett. **35**(21), 3583–3585 (2010).
5. F. Siewert, J. Buchheim, S. Boutet, G. J. Williams, P. A. Montanez, J. Krzywinski, and R. Signorato, "Ultra-precise characterization of LCLS hard X-ray focusing mirrors by high resolution slope measuring deflectometry," Opt. Express **20**(4), 4525–4536 (2012), http://www.opticsinfobase.org/abstract.cfm?URI=oe-20-4-4525.
6. P. Z. Takacs, S. N. Qian, and J. Colbert, "Design of a long trace surface profiler," Proc. SPIE **749**, 59–64 (1987).
7. S. N. Qian, W. Jark, and P. Z. Takacs, "The penta-prism LTP: A long-trace-profiler with stationary optical head and moving penta prism," Rev. Sci. Instrum. **66**(3), 2562–2569 (1995).
8. P. Su, J. H. Burge, B. Cuerden, J. Sasian, and H. M. Martin, "Scanning pentaprism measurements of off-axis aspherics," Proc. SPIE **7018**, 70183T, 70183T-10 (2008).
9. P. Su, J. H. Burge, B. Cuerden, R. Allen, and H. M. Martin, "Scanning pentaprism measurements of off-axis aspherics II," Proc. SPIE **7426**, 74260Y, 74260Y-9 (2009).
10. J. Fleig, P. Dumas, P. E. Murphy, and G. W. Forbes, "An automated subapeture stitching interferometer workstation for spherical and aspherical surfaces," Proc. SPIE **5188**, 296–307 (2003).
11. D. Malacara-Doblado, K. Creath, J. Schmit, and J. C. Wyant, "Testing of aspheric wavefronts and surfaces," in *Optical Shop Testing* 3rd ed., D. Malacara, ed., (Wiley, 2007) 435–497.
12. J. Ojeda-Castañeda, "Foucault, wire, and phase modulation tests," in *Optical Shop Testing* 3rd ed., D. Malacara, ed., (Wiley, 2007) 275–316.
13. A. Cornejo-Rodriguez, "Ronchi test," in *Optical Shop Testing* 3rd ed., D. Malacara, ed., (Wiley, 2007) 317–360.
14. D. Malacara-Doblado and I. Ghozeil, "Hartmann, Hartmann-Shack, and other screen tests," in *Optical Shop Testing,* 3rd ed., D. Malacara, ed., (Wiley, 2007) 361–397.

15. P. Su, R. E. Parks, L. Wang, R. P. Angel, and J. H. Burge, "Software configurable optical test system: a computerized reverse Hartmann test," Appl. Opt. **49**(23), 4404–4412 (2010), http://www.opticsinfobase.org/abstract.cfm?URI=ao-49-23-4404.
16. T. Bothe, W. Li, C. von Kopylow, and W. Jueptner, "High resolution 3D shape measurement on specular surfaces by fringe reflection," Proc. SPIE **5457**, 411–422 (2004).
17. M. Knauer, J. Kaminski, and G. Hausler, "Phase measuring deflectometry: a new approach to measure specular free form surfaces," Proc. SPIE **5457**, 366–376 (2004).
18. M. Sandner, W. Li, T. Bothe, J. Burke, C. v. Kopylow, and R. B. Bergmann, "Absolut-Abstandsreferenz für die Streifenreflexionstechnik zur Verringerung systematischer Messfehler," in Proceedings of DGaO 2011 (2011)
19. F. Ligtenberg, "The moire method, a new experimental method for the determination of moments in small slab models," Proc. Soc. Exp. Stress Anal. **12**, 83–98 (1954).
20. R. Ritter and R. Hahn, "Contribution to analysis of the reflection grating method," Opt. Lasers Eng. **4**(1), 13–24 (1983).
21. D. Perard and J. Beyerer, "Three-dimensional measurement of specular free-form surfaces with a structured-lighting reflection technique," Proc. SPIE **3204**, 74–80 (1997).
22. R. Höfling, P. Aswendt, and R. Neugebauer, "Phase reflection—a new solution for the detection of shape defects on car body sheets," Opt. Eng. **39**(1), 175 (2000).
23. J. H. Burge, P. Su, C. Zhao, and T. Zobrist, "Use of a commercial laser tracker for optical alignment," Proc. SPIE **6676**, 66760E, 66760E-12 (2007).
24. T. Bothe, W. Li, M. Schulte, C. von Kopylow, R. B. Bergmann, and W. P. O. Jüptner, "Vision ray calibration for the quantitative geometric description of general imaging and projection optics in metrology," Appl. Opt. **49**(30), 5851–5860 (2010).
25. P. Su, R. E. Parks, Y. Wang, C. J. Oh, and J. H. Burge, "Swing arm optical coordinate-measuring machine: modal estimation of systematic errors from dual probe shear measurements," Opt. Eng. **51**(4), 043604 (2012).
26. M. Vo, Z. Wang, L. Luu, and J. Ma, "Advanced geometric camera calibration for machine vision," Opt. Eng. **50**(11), 110503 (2011).
27. M. Idir, P. Mercere, M. H. Modi, G. Dovillaire, X. Levecq, S. Bucourt, L. Escolano, and P. Sauvageot, "X-ray active mirror coupled with a Hartmann wavefront sensor," Nucl. Instrum. Methods Phys. Res. A **616**(2-3), 162–171 (2010).

1. Introduction

Focusing light to nanometer length scales and preserving the high brightness made available by third and fourth generation synchrotron/FEL sources requires significant advances in the quality of reflective EUV, soft X-ray and X-ray optics and in the metrology used to optimize their fabrication. The transport and monochromatization of X-ray/EUV light from a high brilliant source to the sample without significant loss of brilliance and coherence is a challenging task in X-ray optics and requires optical elements of very high accuracy [1–4]. These are wavefront preserving plan or highly focusing mirrors with lengths of up to 1 m characterized by residual slope errors in the range of 50 nrad rms and values of 0.3 nm rms or less for micro-roughness [5].

Today, manufacturing techniques allow for figuring arbitrary optical surfaces. The form of these elements can be corrected at the nanometer level by computer controlled polishing or ion beam figuring but the accuracy of absolute form metrology limits the possibilities of the manufacture of modern optical elements. This makes new metrology developments necessary.

The actual state-of-the-art optical instruments available in optical metrology laboratory do not have adequate sensitivity and do not cover a wide range of spatial frequencies to provide the user with useful information necessary to feedback the polishing process to improve the quality of the optical component.

Metrology plays a critical role in modern figuring because computer-controlled figuring is performed using the measured surface profiles. Thus, the key point for fabricating elliptically curved surfaces is the improvement of the metrology, as the measurement accuracy determines the final figure accuracy of the fabricated mirror. The designed instrument will be targeted for the high accuracy metrology of very steep curved aspherical optics not covered (or poorly) right now by the existing technology such as profilometer, interferometer etc.

In this paper, we show how the Software Configurable Optical Test System (SCOTS) can be used to perform high accuracy optical metrology for X-ray mirrors. Different from the scanning type high precision slope metrology such as long trace profiler (LTP) [6,7], scanning pentaprism test [8,9], or interferometric surface topography: subaperture stitching

interferometry [10] and null interferometric test with computer generated hologram or null lenses [11], the SCOTS provides a full field slope measurement of the test surface with a simple non-null configuration. The idea of the SCOTS goes back to the only tests opticians had for measuring topography prior to the laser and computers, namely, slope measuring tests such as the knife edge, the Ronchi test [12,13], the Hartmann test (1900), Shack-Hartmann test [14] etc. The SCOTS is based on the rich developments of the reflection deflectometry [15–18]. Ligtenberg introduced the reflection moiré method for the determination of moments in small slab models [19]. Reflection grating method introduced by R. Ritter simplified the test geometry for slope measurement using one grating and its image [20]. The techniques were further advanced as the structured lighting reflection techniques [21]. Furthermore, phase shifting algorithms are used for data reduction [22]. Originally, the SCOTS was developed for measuring solar concentrators and then applied for testing mirrors for astronomical telescopes at different stages of fabrication. Our recent development has concentrated on improving the test performance to nm level for precision optics.

This paper is organized as follows. In Section 2, we outline the mathematical description of the technique and the principle used, in Section 3 we describe its applicability to problems related to X-ray optics metrology and show some metrology results and discussion. Finally, conclusions and perspectives are drawn is Section 4 and 5.

2. Mathematical description and principle of SCOTS

As mentioned before the SCOTS was based on the geometry of the fringe reflection/ phase measuring deflection [7–8,15] for rapidly, robustly, and accurately measuring large, highly aspherical shapes such as solar collectors and primary mirrors for astronomical telescopes. The detailed principle of the SCOTS is shown in [15] and summarized below. In the SCOTS's simplest configuration, all that is needed to perform the test is a laptop computer with a built-in camera. The laptop illuminates the test surface with a light pattern on the LCD screen and uses the reflected image to determine the surface gradients.

2.1 Reverse Hartmann test, triangulation and centroiding model

The SCOTS can be better understood as doing a traditional Hartmann test with the light going through the system in reverse: see Fig. 1(a) and 1(b). Figure 1(b) shows schematically how the surface slope is measured and calculated. The flat display is set up with its screen near the center of curvature and facing the mirror under test. If a single pixel is lit up on the otherwise dark screen, the image of the mirror, which is captured by the camera's CCD detector, will show a bright region corresponding to the area on the mirror where the angle of incidence from the bright pixel on the screen is equal to the angle of reflection back to the camera. The angular bisector of the incident and reflected rays is normal to the surface at the bright point. The surface slopes (w_x and w_y) at the bright points can be calculated based on triangulation using the coordinates of the lit screen pixel, the camera aperture center, and the reflection of the illuminated pixel as shown in Eq. (1). The slopes can be integrated using a polynomial fit to the slopes or by zonal integration method to give the surface shape (w):
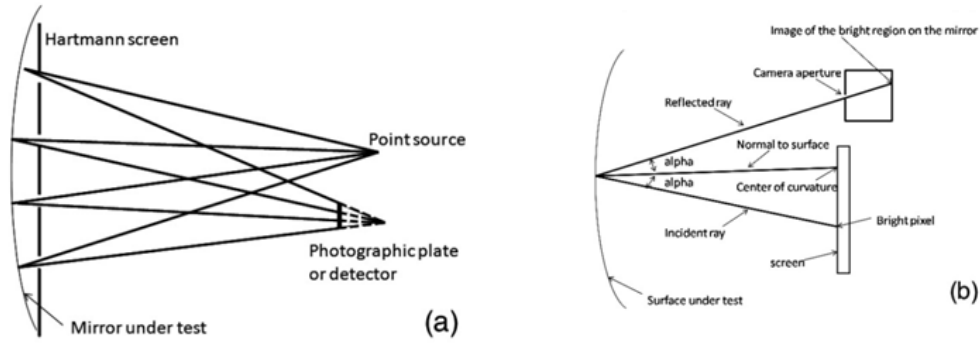
Fig. 1. Comparison of the test geometry for (a) a Hartmann test and (b) the SCOTS.

$$w_x\left(x_m, y_m\right) = \frac{\dfrac{x_m - x_{screen}}{d_{m2screen}} + \dfrac{x_m - x_{camera}}{d_{m2camera}}}{\dfrac{z_{m2screen} - w\left(x_m, y_m\right)}{d_{m2screen}} + \dfrac{z_{m2camera} - w\left(x_m, y_m\right)}{d_{m2camera}}}$$

$$w_x(x_m, y_m) = \frac{\dfrac{y_m - y_{screen}}{d_{m2screen}} + \dfrac{y_m - y_{camera}}{d_{m2camera}}}{\dfrac{z_{m2screen} - w\left(x_m, y_m\right)}{d_{m2screen}} + \dfrac{z_{m2camera} - w\left(x_m, y_m\right)}{d_{m2camera}}} \tag{1}$$

where x_m and y_m are the coordinates of the test surface that can be obtained from the calibrated mirror image (bright region); x_{camera} and y_{camera} are the coordinates of the camera that can be obtained from geometric measurement of the test setup; x_{screen} and y_{screen} are the coordinates of the bright screen pixel that can be calculated by centroiding or phase shifting methods; $z_{m2screen}$ and $z_{m2camera}$ are the z coordinate differences between the mirror and the screen and between the mirror and the camera; $d_{m2screen}$ and $d_{m2camera}$ are the distances between the mirror and the screen and between the mirror and the camera; and $z_{m2screen}$, $z_{m2camera}$, $d_{m2screen}$, and $d_{m2camera}$ can be obtained from geometric measurement and calibration.

In a Hartmann test a point source of light at the center of the curvature reflects off the surface being tested. The pupil is divided into numerous sample regions with a mask, and the light from each of these regions refocuses on a detector. The positions of the refocused light spots indicate the slope of the surface in each of the regions, and these slopes can be compared with those for a theoretically perfect surface. In the SCOTS, it is useful to visualize the system backward, where the rays start from the camera aperture, hit the mirror, and reflected towards the screen. Now the screen has the function of the detector in the Hartmann test, while the camera works as the point source. Moreover, because the camera takes the pictures of the mirror during the test, it also supplies information about the pupil coordinates (measurement positions at the mirror), which correspond to the Hartmann screen hole positions. Each illuminated camera pixel samples a certain region of the test mirror. We call this region the mirror pixel for convenience in the following discussions. With a finite size of the camera aperture, multiple screen pixels can light up the same mirror pixel. Analogous to the Hartmann test, the average slope at a mirror pixel can be measured by evaluating the centroid (first moments) of the corresponding screen pixels with Eq. (2) and then substituting the centroid values back into Eq. (1):

$$x_{screen} = \frac{\sum\limits_{i \in ESP} x_i I_i}{\sum\limits_{i \in ESP} I_i}, \quad y_{screen} = \frac{\sum\limits_{i \in ESP} y_i I_i}{\sum\limits_{i \in ESP} I_i} \tag{2}$$

where the centroid of the screen pixels (x_{screen}, y_{screen}) can be calculated from a light intensity weighted average using effective screen pixels (ESPs). The ESPs are all the pixels that can light up a certain mirror pixel. Pixel light intensities can be read out from the camera pictures.

The centroiding process supplies sub-pixel slope measurement which provides the high slope sensitivity of the test. The reverse Hartmann geometry replaces the relative small format detector with large size screen, which provides an enormous large dynamic range for the test. Using the camera mapping the test surface, this significantly increases the test surface measurement sampling than the traditional Hartmann test.

2.2 Synchronous detection

Based on the former discussions, we need to determine the correspondence between the screen pixel location and a certain mirror pixel to do the triangulation calculation. This can be done efficiently by coding the screen pixels. A common way to do this is to code the screen pixel with intensity variation: displaying sinusoidal fringes on the screen. By phase shifting the fringes and taking pictures, the phase value that corresponds to a screen pixel coordinate at a certain mirror pixel can be found by synchronous detection techniques. See Ref [15]. for further discussions.

2.3 Transverse ray aberration model

For a smooth test surface, triangulation in Eq. (1) can be done by knowing camera pinhole position, screen pixel positions and at least one point on the test surface where usually the position of the vertex of the test surface is known. In many cases of testing a polished spherical or aspherical optical surface, the surface geometry is close to the ideal with microns or less surface shape departure. The relative positions between the test surface, the camera and the screen are well controlled during the alignment, for instance with a distance measuring interferometer such as a laser tracker [23]. In this situation, the measurement model can be simplified as a comparison between the ideal transverse ray aberration distribution with the measured transverse ray aberration from the screen centroiding or phase shifting calculation. The transverse ray aberration can be transferred to system wavefront aberration with Eq. (3).

$$\frac{\partial W(x, y)}{\partial x} \cong -\frac{x_{screen}}{d_{m2screen}}, \quad \frac{\partial W(x, y)}{\partial y} \cong -\frac{y_{screen}}{d_{m2screen}} \tag{3}$$

Where $W(x,y)$ is the wavefront aberration, x and y are exit pupil coordinates of the system. The slopes can then be integrated using a polynomial fit to the slopes or by zonal integration method to give the wavefront and further the surface departure from the ideal shape.

2.4 Tradeoff between spatial resolution and slope sensitivity

The test spatial resolution, δx, and slope sensitivity, $\tan \delta \alpha$, have a relation with system light wavelength, λ, and system quality factor Q as shown in Eq. (4) [17].

$$\tan \delta \alpha \bullet \delta x = \frac{\pi \lambda}{Q} \tag{4}$$

We demonstrated that in the experiment that 0.1µrad rms slope precision can be obtained by achieving a high Q factor with a spatial resolution at a few millimeter level.

3. Application of the method to X-ray optics metrology

3.1 SCOTS test of a long radius spherical mirror

Using the SCOTS, We tested a high precision spherical sample mirror provided by Brookhaven National Laboratory. The mirror has a size of $100 \times 30 \times 40$mm, and a radius of 54.29m (measured from a LTP which can measure surface slope to ~0.1 µrad rms).

The mirror was measured with the SCOTS using the equipment shown in Fig. 2. The components were mounted on an optical rail on a standard laboratory bench. No environmental control other than the buildings air-conditioning system (20°C ± 0.5, 50% relative humidity) was required during the measurements reported in this work.

In our setup, a 19" LCD screen is used as the illumination source to generate sinusoidal fringe patterns for synchronous detection. A CCD with a focal length of 50mm camera lens sits next to the LCD screen. The camera and the screen is ~3m away from the test optics. A spatial filter is put in front of the camera to remove the pupil imaging aberration of the camera lens as explained in Sec.3.3.2.
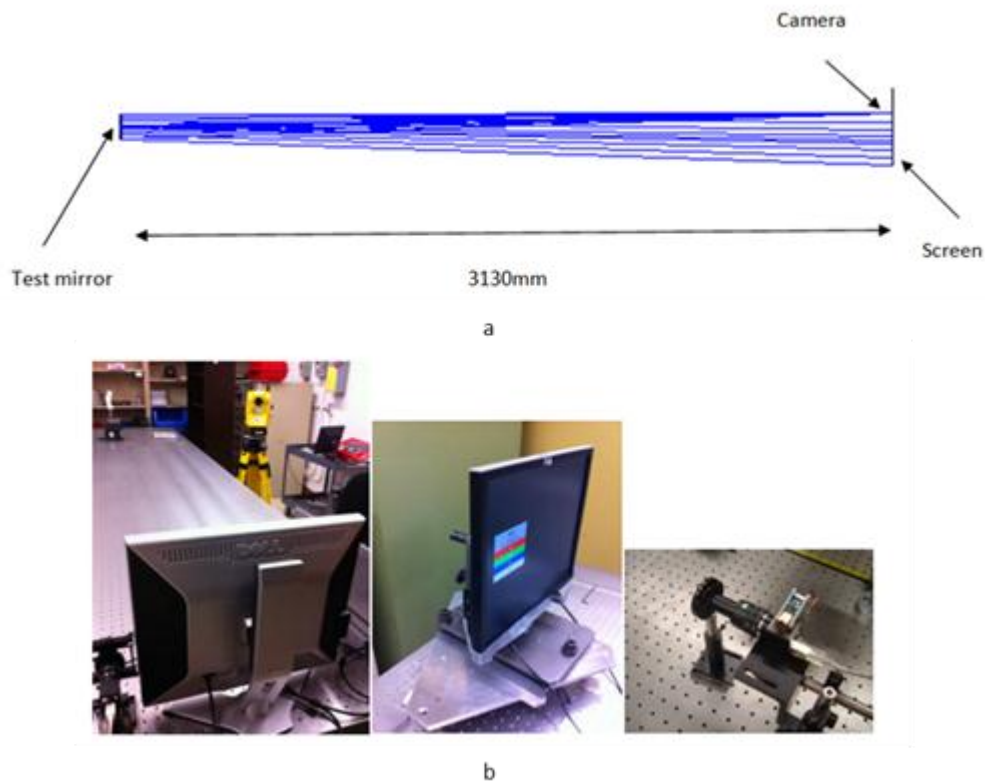
Fig. 2. Geometric layout (a) and experiment setup(b) of the SCOTS test for the spherical mirror.

Sixteen step phase shifting was used for data collection and reduction. Figure 3 shows one of the sets of the collected fringe data.
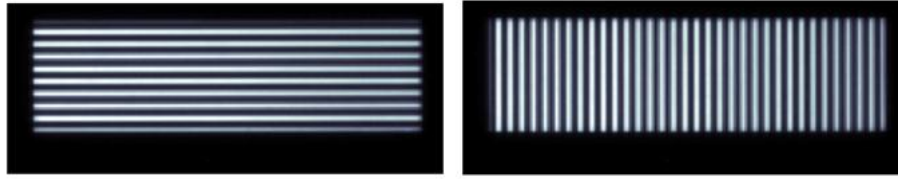
Fig. 3. The fringe data of the SCOTS.

Next, the fringe data was processed to find the phase, which was unwrapped to find the slope data. Figure 4 gives the unwrapped slope data from the test, where the unit is in radians.
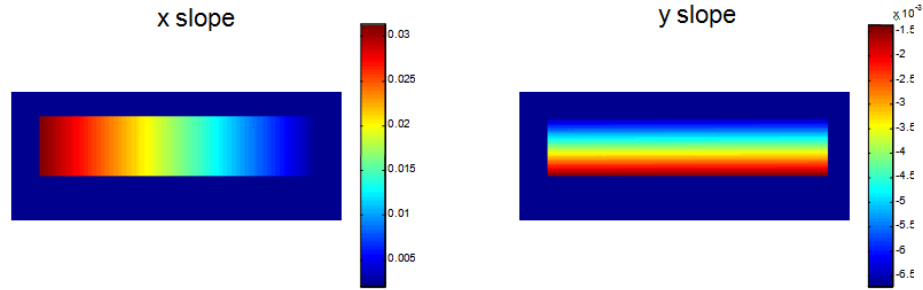

Fig. 4. Unwrapped slope data in x and y directions (unit: radian).

Last, the shape of the surface was calculated through integration of the x and y slope data. Figure 5 shows the shape with the power and astigmatism removed, where the rms error of the surface is 8nm. This surface rms includes the surface shape, the systematic errors from the test geometry and the errors induced from the imaging aberration of the commercial lens being used. The test accuracy can be improved by accurately measuring the system geometry, for instance with a laser tracker and also with a customized high quality camera lens.
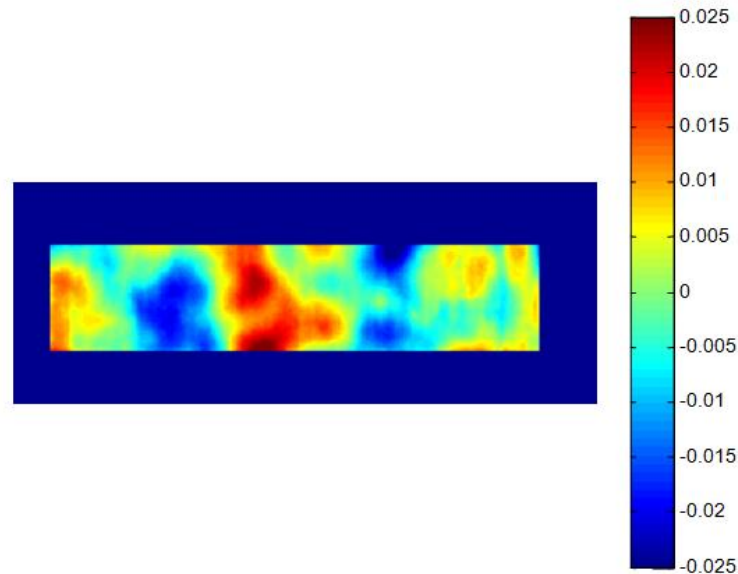

Fig. 5. Integrated surface data, rms = 8nm (unit: micron).

Figure 6 shows that ~0.1 µrad slope noise level was achieved by data averaging. Data from each phase shift was an average of 2048 single images with a total exposure time of 68 seconds per step.
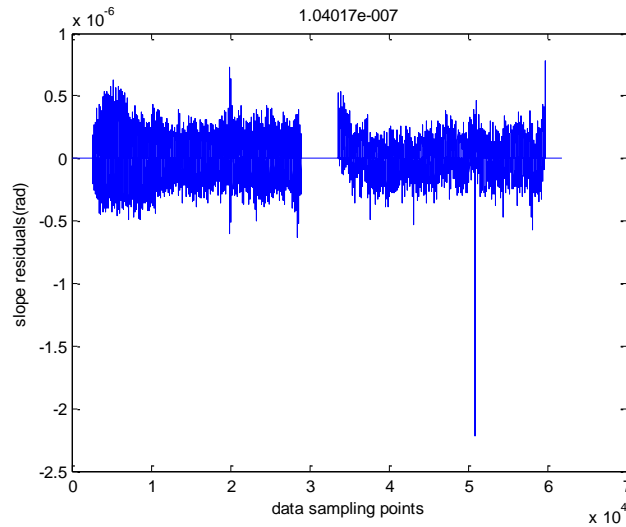

Fig. 6. Slope residuals are ~0.1 µrad from the integration process.

3.2 Calibration of the test with a plano mirror

The SCOTS system can be calibrated to eliminate the system errors. The calibration can be conducted with a known flat optical surface measured by interferometry. This was done for our test system with a 4" interferometer reference flat. The data of the flat shows a peak-valley of 20 nm power, 40 nm astigmatism and 2 nm rms other surface errors. After taking a measurement of the test sphere, the reference flat was setup into the SCOTS test cavity by controlling the flat position to ~100 micron and tip/tilt to ~1 arcmin by using indicators. Figure 7 shows an example of the measured fringe from the flat. Figure 8 shows the integrated surface map and interferometric data from the flat, both with power and astigmatism removed. The difference of the two maps is the systematic errors and effects in this particular SCOTS system to be calibrated with the flat data.
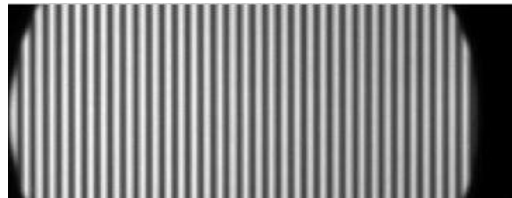

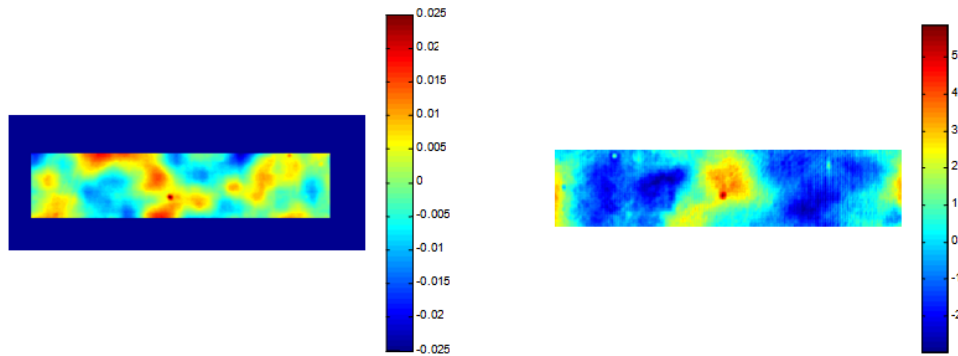
Fig. 7. An example of the measured fringe from the flat.

Fig. 8. The integrated surface from the flat (left, unit: micron) interferometric data for the flat (right, unit:nm), both with power and astigmatism removed.

Figure 9 gives the estimated test sphere map by subtracting flat data from the sphere measurement. The surface radius calculated from the power map is 54.15m over the sampled aperture size of 90mm in the long end.
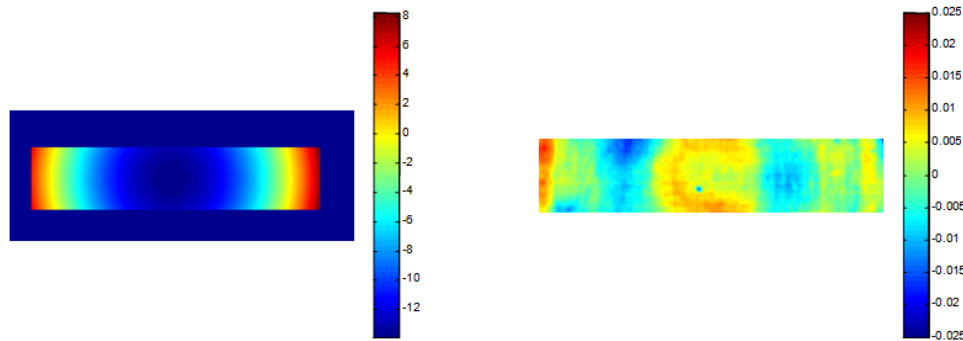

Fig. 9. Sphere surface map with power rms = 6 micron, calculated radius R = 54.15m; surface map without power and astigmatism, rms = 4nm. Calibration from the flat is applied (unit: micron).

Figure 10 shows the measurement result from LTP, the height errors are ~3.4nm rms with the comparison of the center line profile from the SCOTS. We can see the excellent performances achieved by the SCOTS system compared to the LTP measurement. The difference between the two tests methods can come from the following sources: 1) uncertainty from both test methods, 2) registration uncertainty between the SCOTS map and the LTP profile, 3) the system stability induced fringe print-through errors, which will be described in the Sec. 3.3.4.
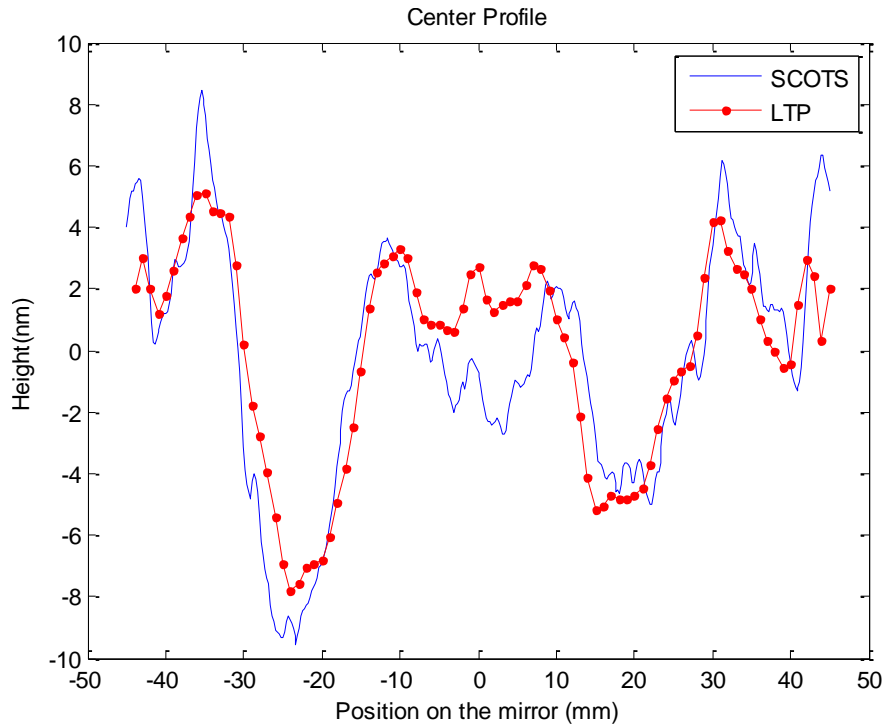
Fig. 10. The center line profiles of the test sphere from the SCOTS and LTP measurement.

3.3 Test uncertainty analysis

In this section, we discuss the SCOTS test uncertainties by considering the uncertainty contributed from the properties of the system components, which are the imaging camera and the illumination screen, and also the alignment effects from the test.

3.3.1 Sensitivity to camera mapping distortion

The effect of the mapping errors due to the camera distortion is proportional to the derivative of the test system slopes, where the cross derivative terms are usually small. The mapping sensitivity was ~0.2mrad/ mm (0.05mrad/pixel) when testing the sphere. When calibrating the test with the flat reference, we are actually looking at the departure from the flat. The mapping sensitivity is significantly reduced to ~0.018mrad/ mm (4μrad/pixel). A calibration of the camera distortion to ~0.01pixel rms will introduces only 0.04μrad slope errors. In our experiment, the camera distortion was calibrated to ~0.01 pixel with markers generated from a LCD screen which was aligned to be parallel to the test part. In general, for the situation when the test part geometry is significantly far from a flat, ray tracing method can be used to propagate the test coordinates from the calibration plane to the curved test surface, which was done in one of our applications for measuring an F/4 off- axis parabolic mirror.

3.3.2 Effect from lens pupil aberration

The SCOTS reverse Hartmann model described in Sec. 2.1 assumes an ideal pinhole camera model such that the location of the pinhole is needed for the triangulation calculation. For an arbitrary camera lens system, this assumption is not always satisfied. This effect is illustrated in Fig. 11 for a camera lens with a general Double Gauss type design. Lights from different field angle will pass through a same point, the center of the lens aperture stop. However at entrance pupil (image of the aperture stop) in object space, which can be located by extending

the chief rays from different fields and finding out the minimum intersection plane, the light will not converge to a single point due to the lens pupil imaging aberrations. Figure 12 gives the ray displacement at the pupil plane as a function of the lens field angle. The peak-valley of the displacement is ~0.35mm, which generally cannot be ignored in the triangulation calculation.
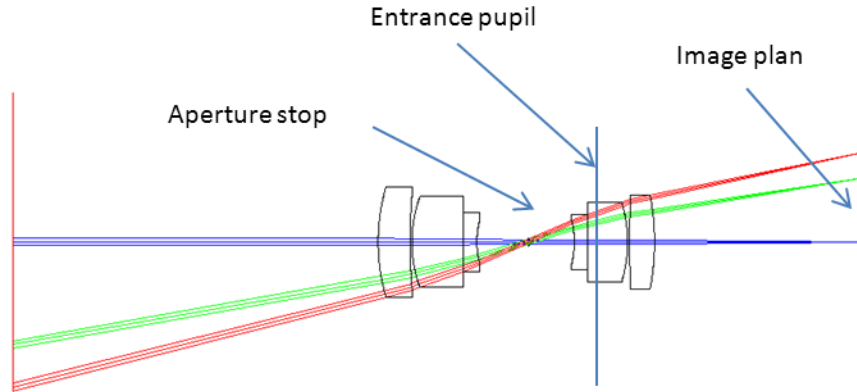

Fig. 11. Layout of a Double Gauss type camera lens design, which illustrates the effect of the pupil aberration.
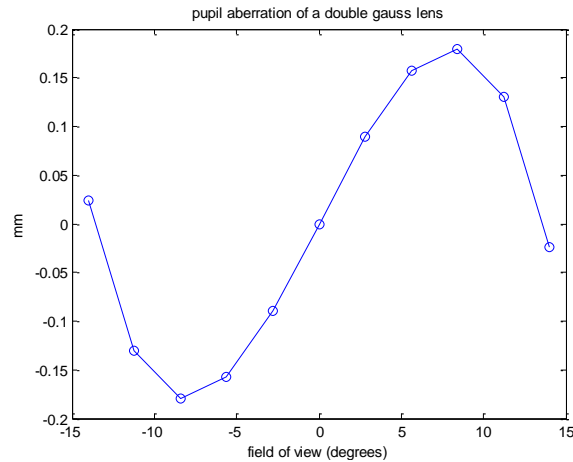

Fig. 12. Pupil aberration effect: ray displacement at the pupil plane as a function of the lens field of view.

The entrance pupil, which is the image of the internal stop, has different locations and shapes considering light from different field angles. This effect violates the pin-hole camera model for the SCOTS test. The lens pupil aberration effect can be taken care of by using a multiple view points (MVP) camera model, and can be experimentally calibrated to a certain level [24]. We removed the pupil aberration effect inherently by using camera lens with an external stop in front of the lens. In this way, the location and the shape of the stop is well defined. Experiments shown in the paper required only a small field of view for the camera lens; a commercial lens with an external stop was used. The internal stop of the lens was

opened to the maximum so that the external iris was the true stop of the lens. Because the lens was working at a large F/#, the aberration variation due to the stop shift was insignificant. For our other test applications where a large field of view is required, special type camera lens and customized lens have been used.

3.3.3 Effect from lens imaging

As seen from test data and screen flip experiment data shown in Fig. 13, the dominant errors in the test without the reference calibration are from the lens imaging effect. The effect of the imaging aberration to the test can be simulated by putting the lens design model into the SCOTS test reverse ray tracing model. The current test uses a commercial imaging camera lens. By using the reference calibration, the majority of the induced errors are removed. However as the test surface significantly departs from the shape of the reference, a high-quality customized lens is preferred. Effects from ghost imaging, scatter light, dust, lens local defects can also be simulated with the model mentioned above as well.

3.3.4 Effect from the screen substrate shape errors

An area with more than 200mm in the long end at the screen was used for illumination during the test. Screen substrate shape was measured with an optical coordinate measuring machine, which showed a dominant shape error of peak-valley of ~200μm in quadratic form. As can be seen from test layout shown in Fig. 2, the maximum light angle relative to the screen is ~2degrees. To check the effect from the illumination screen, we flipped the screen 180degrees and took another set of measurements with average of 256 images. The test map difference before and after rotating the screen is 0.6nm rms and shows some fringe print through errors due to the system instability. Further experiment will be performed to understand and reduce this effect.
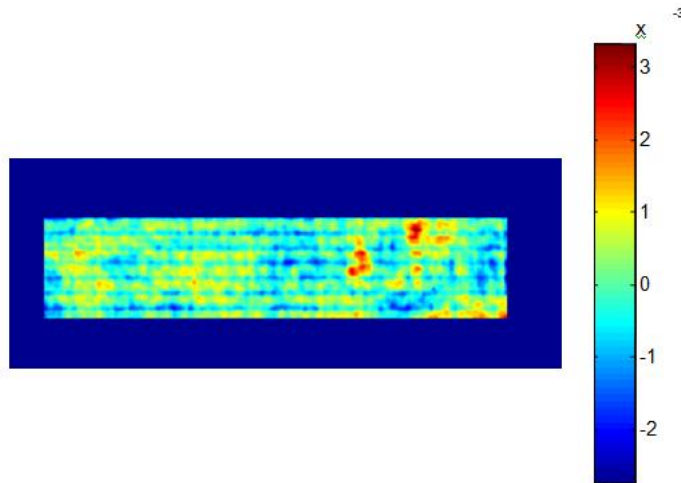

Fig. 13. Test difference before and after rotating the illumination screen 180degs, rms = 0.6nm (unit: micron).

The error from the screen is insignificant in this case. Normally the induced pixel position errors seen by the test light is proportional to the light angle and the screen substrate departure from a flat. So the test errors become larger as the test part gets faster (smaller F/#). However by doing a relative measurement, for instance calibrating with a flat reference, the induced pixel position errors are only proportional to the local substrate departure between the test beam and reference beam position assuming small angle difference between the two beams. Therefore the sensitivity to the screen errors is significantly reduced.

3.3.5 Effect from system geometry and alignment

The system geometry can be measured accurately with a laser tracker, a 3D coordinate measuring machine. Positions of the camera pinhole aperture, screen pixels and the test part can be calibrated into the tracker coordinate system with a procedure similar to the one described in Ref [25]. An uncertainty of 0.025mm is reasonably achievable and can be further improved with careful calibrations. The effect to the geometry uncertainty is then modeled and analyzed in optical design software. For instance, for the 4" reference flat SCOTS test, a 0.1mm lateral position uncertainty of the camera pinhole position introduces 0.25nm surface astigmatism. Effects from screen alignment, such as tip/tilt, are cancelled out during the reference calibration process.

3.3.6 Summary of test uncertainties

The detailed experiment uncertainties are summarized in Table 1.

Table1. Experiment Uncertainties for Measuring the Test Sphere with the SCOTS

Error sources	Uncertainties	Effect to the measurement
Camera imaging distortion	0.01 pixel	0.04 μrad slope errors
Camera pupil aberration	Removed with external stop	ignorable
Camera imaging aberration, ghost imaging, scatter light, dust, lens local defects	Removed by calibration with a reference flat	ignorable
Screen pixel pitch (scaling effect)	Calibrated to 10^{-5}	ignorable
Screen substrate shape errors	P-V ~200 microns, light angle less than 2 degrees	ignorable
Light intensity angular effect	Noticeable over a large region, and neglect able within the small angular range for centroiding calculation	ignorable
Light intensity nonlinearity	Effect removed by multi step phase shifting	ignorable
Geometry and alignment: camera pinhole location screen location screen tip/tilt and rotation the SCOTS clocking to the test part	Calibrated with a laser tracker ; Removed by calibration with a reference flat	ignorable
Phase calculation	Average of multiple measurements	0.1 μrad repeatability
Environment instability and noise	To be addressed in the future	0.6nm

4. Perspectives: metrology of high quality aspherical X-ray optics and active optics calibration

As stated in our introduction, focusing X-ray beams from modern synchrotron radiation sources is one of the key technical challenges in the growing field of X-ray microanalysis and microscopy. The target in polishing reflective optics is really to reach diffraction limited performances for x-ray mirror (fen nm rms height errors and highly off axis elliptical mirror). Preliminary experiment results demonstrated in this paper shows that a 0.1 μrad rms slope measurement precision has been achieved with the SCOTS. By further improving the system Q factor in Eq. (4), a target of 50 nrad or less is believed to be achievable.

With the reference flat calibration, not only the surface waviness, but also the absolute shape of the test surface, for instance the radius of curvature, can be measured in high accuracy. In this experiment, we measured the surface slopes to ~0.2 μrad rms in accuracy. Results can be further improved with careful reference flat map calibration and registration, fine tuning the phase shifting process and controlling the environment vibration to remove fringe print through, etc.

The error contribution from the illumination screen can be ignored for long radius optics, which is most of the case for X-ray mirrors. A calibration of the test system with a known

surface which can be a flat or sphere can significantly release the quality requirements on the components for the test system and the knowledge of the test geometry.

Based on the mapping sensitivity analysis, a high-quality imaging lens with careful control of imaging distortion, pupil aberration, imaging aberration, straight light, ghost images and cleanness is desirable for the absolute shape measurement when the test surface is significantly departure from the reference, or when the surface slope variation is significant to introduce mapping errors.

The analysis described in Sec. 3.3 is general. We applied it for a 150mm diameter tangential elliptical X-ray mirror which has maximum sag of 200 μm. The analysis shows that the SCOTS can measure the mirror to less than 0.05μrad in accuracy by optimizing the imaging camera and controlling the distortion to 0.01 pixel rms [26]. Further experiments on it are planned and the results will be reported in the future.

The SCOTS can also be used for x-ray active optics calibration where a mirror is shaped in a targeted profile using two or several actuators like the mirror described in [27].

5. Conclusions

We have demonstrated the successful applications of the SCOTS to rapidly and robustly measure the profile of an X-ray reflective optics. This new, simple, non-contact measurement system offers the characteristics desired for a high-end, single-piece, freeform optics metrology tool: high accuracy, universal, non-contact, large measurement volume and short measurement time). Future calibrations and development of the control and data-processing software will certainly further improve the potential performances of this technique. In this work, we demonstrated the technology ability with measuring a spherical surface. However the test principle and the analysis described in the paper are general and can be applied to aspheric or free-form optical surfaces.

Acknowledgments